Journal of Materials Chemistry A

Accepted Manuscript

ROYAL SOCIETY OF CHEMISTRY

www.rsc.org/materialsA

Journal Name

ARTICLE

Silica direct evaporation: A size-controlled approach to SiC/carbon nanosheet composites as Pt catalyst support for superior methanol electrooxidation

Received 00th January 20xx,
Accepted 00th January 20xx

DOI: 10.1039/x0xx00000x

www.rsc.org/

Lei Wang,[a] Lu Zhao,[a] Peng Yu,[a] Chungui Tian,[a] Fanfei Sun,[b] He Feng,[a] Wei Zhou,[a] Jianqiang Wang[b] and Honggang Fu[a,*]

Carbides have been regarded as a kind of promising supports to improve the utilization of Pt for anode catalyst in fuel cells owing to its Pt-like property. Unlike other carbides, the relevant studies about SiC are scarce because the effective synthesis is challenging from a small size and high performance. Herein, we develop a novel and facile vapor deposition strategy to synthesize the nanocomposite composed of 17 nm SiC nanoparticles uniformly dispersed on graphitic carbon nanosheets (namely SiC/GC) derived from silica ceramic chip and coconut shell-Fe^{3+} (CS-Fe^{3+}). In the synthesis, the CS-Fe^{3+} was transferred to GC firstly, and then the silica vapor from ceramic chip could deposit on GC, meanwhile, the reduction of silica to SiC would occur and the SiC/GC composite was obtained. Because of the synergistic effect and unique structures, the as-prepared Pt-SiC/GC with a low loading of 10 wt% Pt exhibits the superior activity of 1585.3 A g^{-1} Pt towards methanol electrooxidation, which is about 6.2 and 5.0 times as that of the commercial 20 wt% Pt/C(JM) and 30 wt% PtRu/C(JM) catalysts, respectively, combining with larger ECSA, better stability and superior CO stripping.

1. Introduction

Electrochemical energy conversion devices, especially direct methanol fuel cells (DMFCs), have attracted much interest in stationary and mobile applications due to their high volumetric energy density, and their ease of storage and transport compared to the hydrogen fuel cells.[1-6] However, the anodic methanol oxidation reaction (MOR) shows different low-efficiency oxidation path by adopting non-precious metal catalyst. Therefore, the high-cost precious metals Pt employed as the irreplaceable catalysts in the anodic methanol oxidation reaction (MOR) is the biggest obstacle for the commercialization of DMFCs.[7,8] Pt black or 2~5nm Pt nanoparticles (NPs) dispersed onto a carbon black support (Pt/C) are the current state-of-the-art electrocatalysts.[9,10] Although these catalysts exhibit excellent initial electrocatalytic activity, the poor kinetic and poisoning characteristic of Pt by surface-adsorbed intermediate species of MOR (such as CO and CHO) would lead to a low life-time.[11-14] To address the above issues, intensive studies have been devoted to Pt alloying, frameworks and high-index facets.[15-21] Notably, these Pt-based catalysts still suffer from complicated synthesis and high-cost, dissolution and Ostwald ripening/aggregation under the operating conditions especially in acid electrolyte, leading to a fast decay of the catalytic performance. Hence, lowering the usage but promoting the performance of Pt is the present research focus.

Alternatively, the interstitial compounds of carbides and nitrides inspire the passion of developing novel supports for lowering Pt loading in DMFCs due to their Pt-like property, electrochemically and thermally stability, exceptional hardness and corrosion resistance.[22-28] More importantly, the electron transfer between carbides (nitrides) and Pt NPs would be beneficial to the CO desorption, which could reduce the poisoning of Pt. Recently, we found that the size of carbides (nitrides) play the crucial role for electrocatalytic performance, which could importantly affect the electron transfer and close contact between Pt and carbide (nitride) NPs.[29-31] For a certain quality of carbide (nitride), the small-sized NPs exhibit a higher effective surface area for contacting with Pt and have a higher surface energy for the epitaxial growth of Pt, resulting in larger power energies of fuel cells. On the contrary, large-sized carbide (nitride) NPs have a poor contact with Pt, which could lead to an inferior performance.

In the past years, most of the relative studies focus on the transition metals of W, Mo and V, but the corresponding study about silicon carbide (SiC) is scare. SiC is a wide bandgap

[a] Key Laboratory of Functional Inorganic Material Chemistry, Ministry of Education of the People' s Republic of China, Heilongjiang University, Harbin 150080 (P. R. China); Fax: (+86) 451-86661259; E-mail: fuhg@vip.sina.com
[b] Shanghai Synchrotron Radiation Facility (SSRF), Shanghai Institute of Applied Physics, Chinese Academy of Sciences, Shanghai, 201204, P. R. China
† Footnotes relating to the title and/or authors should appear here.
Electronic Supplementary Information (ESI) available: XPS, XRD, TEM, EDS, TG, EXAFS analysis, Scheme about formation mechanism and electrochemical performance measurements for SiC/GC composites are included. See DOI: 10.1039/x0xx00000x

refractory material that can be widely used in high power electronics and photonic devices.[32] Its electrocatalytic support performance is developing because of the nanosize SiC possesses high mechanical strength and stability in oxidative environments.[33] However, the performances of SiC NPs as supports for Pt NPs are not well as those of the other transition metals carbides (nitrides), which should be attributed to the larger size of SiC NPs limits the effect contact with Pt and decrease the power densities for fuel cell in practical application owing to the high density of SiC materials. For the larger size SiC NPs, more number of SiC will be need to the well contact and produce the synergistic effect with Pt NPs, leading to a bad activity for unit mass catalyst and a low power density for the whole fuel cell. Various synthetic approaches to nanosize SiC have been reported, including thermal reduction of silica–magnesium–carbon system in argon,[34] ion beam implantation of C ions into Si,[35] template technique by using polymethylsilane as a precursor,[36] chemical vapor deposition methods based on tetramethyl silane.[37] Unsatisfactorily, all the obtained SiC NPs show a large size, meanwhile, all the above methods are not favorable for a large-scaled applications because of their quite expensive, complex and low yield. Even the feasible carbothermal reduction route by using SiO_2 nanospheres or Si NPs is still difficult to realize the small size of SiC that below 50 nm, more importantly, the weak contact between SiC and carbon support is not favorable for the development of synergistic effect.[38] Based on the above analyses, we want to develop a facile strategy for preparing high efficient and small-size SiC-based electrocatalytic support by a silica direct evaporation route. Additionally, it is imperative to ensure electronic conductivity of the supports for benefiting the electrons transfer in the MOR, which is also essential in the application of Pt supports. Two-dimensional (2D) graphene nanostructures are considered as the ideal supports for Pt catalyst because of the astonishing conductivity and excellent catalytic activity. Coconut shell (CS), a biomass from the nature, has attracted much attention for synthesis of carbon-based nanostructures due to its plentiful, low cost and renewability, especially for the 2D graphene-like nanosheets derived from the layered structure cementite.[39] As far as we know, there is no effective synthesis reported to control the composition of graphene-like nanosheets-based SiC nanomaterials derived from biomass on a large scale by a facile route.

Herein, we report on a synthesis of uniform and small-sized SiC NPs grown on graphitic carbon nanosheets (SiC/GC) composite by a vaporization-deposition-reduction route. In the synthesis, the biomass of CS coordinated with Fe^{3+} (CS-Fe^{3+}) and the ceramic chip containing silica composition were employed as the carbon and silicon raw material, respectively. During the thermal treatment under argon ambient, the CS-Fe^{3+} gradually transferred to GC at a relative lower temperature that could be proved by X-ray absorption fine structure (XAFS) spectra. Subsequently, the silica vapor derived from ceramic chip could deposit on the synthetic GC at a relative higher temperature. Simultaneously, the deposited silica was reduced to SiC NPs by an in-situ carbothermal reaction, so the SiC/GC composite was obtained. Fine-tuning of saturated vapor pressure by controlling the heating temperature, the content and size of SiC NPs in the synthetic composites could be controlled. The ceramic chip could easily be separated after reaction, so the present route is readily scalable production. The catalyst prepared by loading Pt onto SiC/GC support was performed for MOR, the composition- and structure-dependent electrocatalytic performance is thoroughly investigated. The composite synthesized from the optimal condition as the Pt support for synthesis of Pt-SiC/GC catalyst is a advanced catalyst with enhanced activity, promoted durability and superior CO stripping for MOR due to intimate contact of Pt and SiC could facilitate to perform the synergistic effect. The Pt–SiC/GC catalyst with a low loading of 10 wt% Pt almost shows highest activity among a series of Pt-based carbide anode catalysts of fuel cells. Compared with previous reports, our present strategy has the following significant advantages for constructing small-sized and high-efficiency SiC-based carbon supports, namely, i) the raw materials are abundant and inexpensive, ii) the synthetic process is easy handling, and iii) the preparation is generally suitable for an industrial scale-up. The present work provides a new avenue in the design of novel high-performance catalysts from a facile and low-cost strategy.

2. Experimental section

2.1 Synthesis of SiC/GC composite

In the synthesis, biomass of coconut shell (CS) and the ceramic chip containing silica composition were employed as the carbon resource and silica resource, respectively. Typically, 6g CS was dispersed into 0.16 M $Fe(NO_3)_3$ solution for 5h with stirring. After pouring out the solution and drying the CS, the CS-Fe^{3+} precursor could be obtained. The precursor and ceramic chip were put into a corundum boat and transferred to a temperature-programmed furnace. The precursor was firstly heated to 700 ^oC for 2 h and then heated to 1400 ^oC for 2 h in argon ambient. Finally, the SiC/GC composite was prepared after treating with 10 % HCl. As compared, the SiC/GC samples derived from 1300 ^oC and 1500 ^oC were also synthesized, which are named as SiC/GC-1300 and SiC/GC-1500, respectively. Besides, the same process was conducted only without ceramic chip to prepare GC for comparison. All the synthetic parameters were displayed in Table S1.

2.2 Pt-SiC/GC Catalyst Preparation

Pt-SiC/GC catalyst was prepared by a sodium borohydride reduction processs. In brief, the synthetic 0.12 g of Pt-SiC/GC composite and 35.8 mg of $H_2PtCl_6{\cdot}6H_2O$ were dissolved in 45 mL deionized water by sonicating for 30 min. Subsequently, the pH value was adjusted to about 10 with 0.1 M NaOH solution. Then, the 15 mL solution containing 66.5 mg $NaBH_4$ was slowly dropped into the above suspension. The suspension was finally filtered, washed and dried at 80 ^oC in vacuum oven to obtain Pt-SiC/GC catalyst with Pt loading of 10 wt%. The catalyst derived from SiC/GC-1300 and SiC/GC-1500 supports were named as Pt-SiC/GC-1300 and Pt-SiC/GC-1500, respectively. The same process was conducted with GC for synthesis of Pt/GC catalyst.

2.3 Characterization

X-ray diffraction (XRD) patterns were tested on a Bruker D8 Advance diffractometer equipped with Cu K_α (λ = 1.5406 Å) radiation and a LynxEye Detector. X-ray photoemission spectroscopy (XPS) analyses were carried out on a Kratos-AXIS UL TRA DLD with Al K_α radiation source. Raman spectra were measured by a Jobin Yvon HR 800 micro-Raman spectrometer at 457.9 nm. Transmission electron microscopy (TEM) characterization was acquired on a JEM-2100 electron microscope (JEOL) with an acceleration voltage of 200 kV. The X-ray absorption spectra at Fe *K*-edge and Pt L_3-edge near the edge structure were collected by a transmission mode by using ion chambers at beam line BL14W1 of the Shanghai Synchrotron Radiation Facility (SSRF) of China. The station was operated with a Si (111) double-crystal monochromator. The data were processed by using the program ATHENA, and all fits of the EXAFS data were performed with the program ARTEMIS.[40]

2.4 Electrochemical tests

All the electrochemical tests were carried out on Princeton (VersaSTAT V3) electrochemical station by a three-electrode system. The glassy carbon electrode with a diameter of 4 mm was used as the working electrode. Pt slice and saturated calomel electrode (Hg/Hg_2Cl_2, SCE) were used as the counter electrode and reference electrode, respectively. The catalyst ink was prepared by ultrasonically dispersing the mixture of 5 mg, 1.5 mL ethanol and 0.5 mL of 0.5 wt.% nafion solution. Next, 5 μL of the catalyst ink was dropped onto a pre-cleaned working electrode. After drying, the catalyst on the working electrode was tested by a weighting method. The adsorption/desorption of hydrogen on metal nanoparticles surface were tested in 0.5 M H_2SO_4 electrolyte. The electrode potential was scanned in the range of −0.2~1.0 V vs. SCE at 50 mV s^{-1}. To evaluate the methanol electro-oxidation activity of the catalyst, the 0.5 M CH_3OH + 0.5 M H_2SO_4 solution was used as the electrolyte. N_2 was bubbled through the solution for 20 min prior to all the electrochemical measurements with the purpose of deaeration. To estimate the durability of the catalysts, the chronoamperometric (CA) experiments were performed at 0.5 V for 20000 s. The CO stripping experiments for all the catalysts was tested as follows. High-pure CO was purged into the electrolyte of 0.5 M H_2SO_4 for 30 min while the working electrode was held at 0.2 V vs. SCE. After that, N_2 was purged into the electrolyte for 20 min to remove the non-adsorbed CO. Then, the CO stripping was performed in the potential range of −0.2~1.0 V at a scan rate of 50 mV s^{-1}.

3. Results and discussion

3.1 Structure characterizations

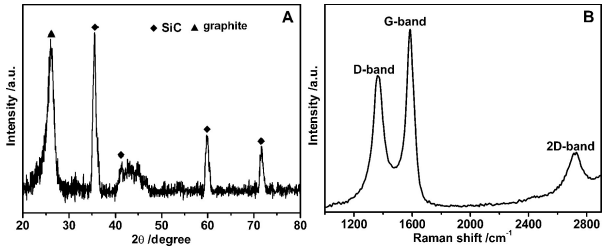

Fig. 1 (A) XRD pattern and (B) Raman spectrum of SiC/GC composite.

The crystalline structures the synthetic SiC/GC composite was firstly analyzed by X-ray diffraction (XRD) pattern. Four reflections at the 35.6°, 41.4°, 59.9° and 71.6° (**Fig. 1A)** are well indexed to the (111), (200), (220) and (311) planes of β-SiC.[30] The peak at 2θ = 26.4° is assigned to the (002) plane of the graphite-like carbon structure. It is demonstrated that the synthetic sample should be composed of SiC and GC.[41] Raman spectrum could further reveal the structures of carbon-based materials. As shown in **Fig. 1B**, the peak at 1585 cm^{-1} (G-band) is assigned to one of the two E_{2g} modes of the stretching vibrations in the sp^2 domains of perfect graphite. The peak at 1365 cm^{-1} (D-band) usually corresponds to the disorder and imperfection of the carbon crystallites. The peak intensity ratio of I_G/I_D for SiC/GC is about 1.3, indicating the formation of GC with well crystallinity, which is consistent with the above XRD results. Besides, the appearance of second-order D peak (2D-band) also implies the existence of GC. X-ray photoelectron spectroscopy (XPS) spectra could provide further information about the composition of the composite. The peaks appeared at 531.7, 284.5, 151.6 and 100.3 eV are ascribed to the characteristics of O1s, C1s, Si2s and Si2p (**Fig. S1)**,[34] respectively, confirming the presence of C, O, Si elements in the sample. It also can be seen from the Fig. S1 that no Fe species is detected. Besides, ICP results also show no Fe species exist in the synthetic SiC/GC sample, implying the complete removing of Fe species. In order to characterize the ash or impurity of CS, we have done the TG analysis of CS raw material under air. As shown in Fig. S2, it can be seen that no residue substances exist after calcination under air, indicating no ash or impurity exists in the CS. Besides, the XPS of the synthetic SiC/GC sample in Fig. S1 also demonstrated no other impurity exists.

The morphologies and microstructures were investigated by transmission electron microscope (TEM). The TEM image in Fig. 2A displays numerous NPs in a uniform size distribution without obvious aggregation dispersed on the carbon nanosheet structures. It should be noted that the carbon layers coating on SiC also can be seen clearly. Such phenomenon is attributed to the synthesized carbon nanosheets can crimp at a higher temperature (1400 ^oC), and the carbothermal process from silica to SiC would make the formation of carbon layer on the surface of SiC NPs. The corresponding size-distributed graph calculated from Fig. 2A has been provided in Fig. S3. It can be seen that the SiC NPs with the size of 10~25 nm, and the average size is about 17 nm. The high-resolution TEM (HRTEM) images (Fig. 1C,D) shows the distinct and continuous lattice fringes with a spacing of 0.252 nm, which is attributed to the (111) planes of SiC.[34] The clear and intensive distinct lattice fringes of GC(002)

plane (0.334 nm) surround the SiC NPs, corroborating the well contact between SiC NPs and GC, which would benefit to developing the synergistic effect. The further enlarged HRTEM images are provided in Fig. S4, and the very clear lattice fringes of SiC(111) can be seen.

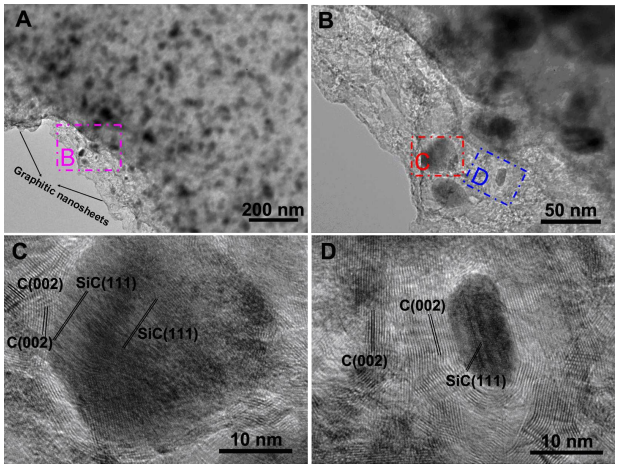

Fig. 2 TEM images of SiC/GC composite with different magnification.

3.2 Formation mechanism

Conventionally, SiC prepared by pyrolysis of carbon containing siloxane polymers at a high temperature of above 1400 °C always displays aggregated and large size.[42,43] However, the SiC/GC composite with highly disperse and small-sized SiC could be successfully synthesized by the present route. An investigation of the formation mechanism of such SiC/GC composite is very significant to the design and synthesis of this type of material for various applications. Our previous studies had been proved that the GC with nanosheets structures could be synthesized by an in-situ self-generating template route.[41,44] Such phenomenon is attributed to the iron species easily form the layered cementite nanostructures, which could be decomposed into Fe and used as the in-situ template for synthesis of 2D carbon structures.

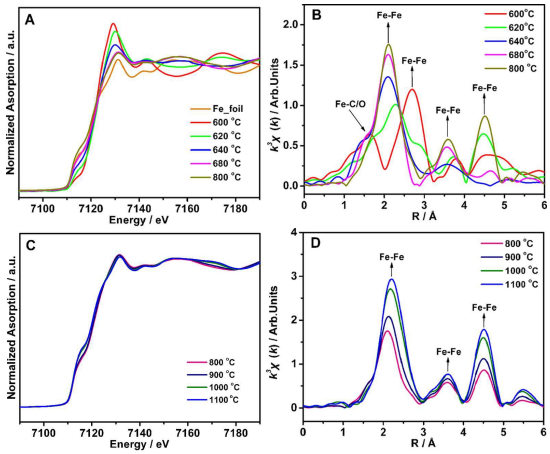

Fig. 3 (A, C) Fe K-edge XANES spectra and (B, D) the Fourier transforms (k^2 weighted) of the composites derived from CS-Fe^{3+} precursor after heating at different temperatures.

To deeply analyze the formation process of the GC nanosheets structures, the changes in the phase and coordination structure of Fe species during the heating process have been studied detailedly by X-ray absorption fine structure (XAFS) spectroscopy. Fig. 3 shows the X-ray absorption near edge structure (XANES) spectra. Based on the R analytic results in Table S1, it can be seen that the Fe elements existed in the form of FeO phase at 600 °C. Subsequently, the FeO phase was gradually transformed into Fe/Fe_3C phase with the improvement of heating temperature. So the Fe element existed in the form of Fe/Fe_3C phase when the heating temperature is 640 °C. The crystalline degree of Fe/Fe_3C is improved with the increase of heating temperature. It can be seen that the crystalline carbon is formed at 700 °C. When the heating temperature is increased to 800 °C, the Fe_3C phase was gradually decomposed into Fe phase, and this decomposition could be finished at 1000 °C. The shift of adsorption edge, the decrease of white line peak and the enhancement of front-edge peak in the XANES spectra also conform to the transformation of FeO-Fe_3C-Fe. The results are consistent with that of XRD patterns in Fig. S5. After the temperature is increased to 800 °C, the raise of front-edge peak could be obviously observed, indicating the increase of electron transition probability. The R analyses demonstrate all the coordination layers belong to the Fe-Fe structure. Then, the peak intensity is gradually increased with further improving temperature, leading to increase the size of Fe particle, and a large size Fe was formed. Finally, the carbon atoms derived from coconut shell could be deposited on the Fe template to form nanosheet nanostructures.

In order to study the transition processes of SiC phase formation, the samples synthesized from CS-Fe^{3+} precursor with different temperature were studied by the XRD patterns. As shown in Fig. S6, the SiC phase was formed at 1200 °C. Additionally, the corundum boat is composed of alumina with the sublimation temperature of 2000 °C, so alumina could not evaporate under the experiment condition for synthesis of SiC/GC. To further prove this, the GC derived from the CS-Fe^{3+} precursor at 1400 °C in a corundum boat without adding ceramic chip was prepared for comparison (the synthetic parameter of GC was displayed in Table S2). The synthetic GC only exhibits the characteristic peaks of crystalline carbon and there is no other phase could be detected (Fig. S7), implying only the silica vapor could produce in the present experiment. The heating temperature greatly affects the vapor concentration of silica, which directly affect the state of SiC NPs in the final samples. The vapor pressure (p) of silica is could be decided by the following Clapeyron equation:

$$\mathrm{Ln}p = \mathrm{A} - \frac{H(v)}{R * Z(v) * T} \qquad (1)$$

Where H (v) is the latent heat of evaporation, Z(v) is the difference between the saturated vapor compression and saturated liquid compression factor, T is the temperature, R is a constant. Both H(v) and Z(v) are constant for a given material, so the above equation could be simplified as lnp = A–B/T. It can be seen that the saturated vapor pressure is increased with the

improvement of temperature. To investigate the formation mechanism of SiC/GC composite, the samples synthesized from different temperatures were also prepared for comparison. Although the SiC/GC composites still could synthesize at a heating temperature of 1300 or 1500 °C (see the XRD patterns in Fig. S8), the size and content of SiC in the samples are different. When the heating temperature was decreased to 1300 °C, the silica vapor is relative less than that of the 1400 °C (Scheme S1), so the large size and aggregated SiC NPs grown on carbon nanostructures could be observed from the TEM images as shown in Fig. S9. This is attributed to the vapor condense in the existence of a small amount of steam environment, which is similar to the principle of water vapor cooled could condense to droplet. When the heating temperature was increased to 1500 °C, the composite with more SiC content could be obtained (see the TEM images in Fig. S10). But the SiC NPs are very large and aggregated compared with that of the SiC/GC synthesized by 1400 °C, because a plenty of silica vapor gradually deposited on the carbon derived from CS at a higher temperature (Scheme S2). The TG results show that the SiC content in SiC/GC composite is increased with the increase of the heating temperature from 1300 to 1500 °C (Fig. S11 and Table S3), which is consistent with the above TEM analyses. Nowadays, various industrial methods to prepare SiC products are employed, including chemical combining approach (Si+C→ SiC), pyrolytic method by using polycarbosilane or methyltrichlorosilane as a precursor, carbothermal reduction route by using SiO_2 and carbon powder, and chemical vapor deposition. However, the size of SiC prepared by the above method is always very large and could not be controlled, which is not favorable for developing the synergistic effect between SiC and Pt NPs. Compared with these, our present method could prepared a small-sized SiC NPs with a average size of 17 nm. More importantly, the content and size of SiC NPs in the synthetic composites could be controlled by tuning of saturated vapor pressure via controlling the heating temperature.

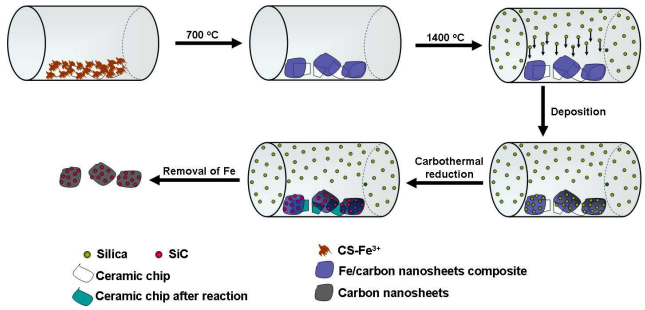

Scheme 1. The proposed formation mechanism of SiC/GC composite.

Based on the above analyses, the formation mechanism of SiC/GC was proposed as Scheme 1. The CS was firstly coordinated with Fe^{3+} ions to form CS-Fe^{3+} precursor. During the followed pyrolysis process, the functional CS gradually transferred to graphitic carbon nanosheets with the increase of thermal temperature. Then, the silica vapor could produce when the temperature is up to the sublimation temperature of the silica in ceramic, and the vapor content increased with the increase of heat treatment temperature. Meanwhile, the silica vapor would deposit on the synthetic graphitic carbon nanosheets and simultaneously reduced to SiC by an in-situ carbothermal reduction reaction, so the SiC/GC composite was obtained. The heating temperature is critical for controlling the content and size of SiC NPs in the resulting SiC/GC composites. This understanding would be meaningful for a controllable design and fabrication the synthesis of other SiC-based nanostructures in different requisite fields.

3.3 Electrochemical performance

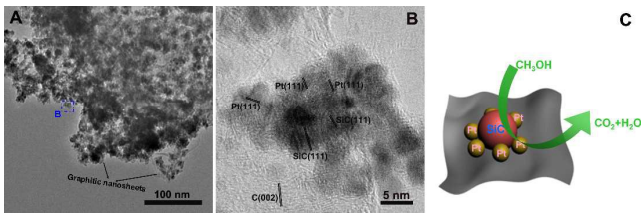

Fig. 4 (A) TEM and (B) HRTEM images of Pt-SiC/GC composite; (C) The structural scheme of Pt-SiC/GC composite.

The GC nanosheets-based composite with small-size carbide NPs can be used as excellent support for Pt catalyst in fuel cells. After loading 10 wt% Pt, the Pt-SiC/GC catalyst could be obtained. It can be seen that Pt NPs are uniformly dispersed on the SiC/GC supports (Fig. 4A). The lattice distance of Pt(111), SiC(111) and GC(002) are identified by the HRTEM image (Fig. 4B). Notably, the intimate contact of Pt NPs, SiC NPs and GC can be distinctly observed, which is favourable for developing the synergic effect (Fig. 4C). The XRD pattern also demonstrated the formation of Pt-SiC/GC composite (see Fig. S12). XPS is a useful technique for confirming the interaction between Pt and SiC in the Pt-SiC/GC composite. The Pt/GC catalyst without SiC was also studied for comparison. As shown in Fig. 5A, the Pt 4f spectrum of Pt/GC displays one doublet with a Pt $4f_{7/2}$ binding energy of 71.3 eV and Pt $4f_{5/2}$ binding energy of 74.6 eV, which is the characteristic of metallic Pt. Importantly, the Pt4f peaks of Pt-SiC/GC exhibit blue-shifted of 0.3 eV (71.6 eV and 74.9 eV) compared with that of Pt/GC, indicating the strong interactions between Pt NPs and SiC NPs. It further demonstrates the existence of electron transfer from Pt to SiC, which is consistent to our previous studies verify the electron transfer phenomena from precious metal NPs to nitrides.[26] The construction of electronic system would be favorable for the CO desorbing during the MOR.

To further investigate the nature of the interaction between Pt and SiC/GC, XAFS spectroscopy was employed. As the XANES of Pt L_3-edge spectra shown in Fig. 5B, both the nano Pt and bulk Pt exhibit the similar resonance patterns above the edge, further demonstrating the fcc structure of Pt NPs. The first resonance of white line arising from 2p→5d dipole transitions for nano Pt exhibits higher energies than the bulk Pt, which is attributed to the nanosize effect.[31] The Fourier transforms of Pt L3-edge extended X-ray absorption fine structure (EXAFS) spectra for Pt-SiC/GC and Pt/GC composites are presented in Fig. S13 and Table S4. Compared with Pt/GC, the higher coordination number of Pt-C in Pt-SiC/GC composite indicates

the more apparent Pt-C due to the intimate contact of Pt and SiC NPs could enhance the interaction between Pt atoms and carbon atoms. Besides, the Pt-Pt coordination number in Pt-SiC/GC (9.84 ± 0.8) is much more close to that of the Pt-Pt in Pt foil (9.22 ± 0.2), implying a higher crystallinity of Pt in Pt-SiC/GC. Given the above, the presence of SiC could improve the crystallinity of Pt, which is associated with the well lattice matching between Pt and SiC benefit to the epitaxial growth of Pt on SiC, like the reported WC-noble metal system.[30,31]

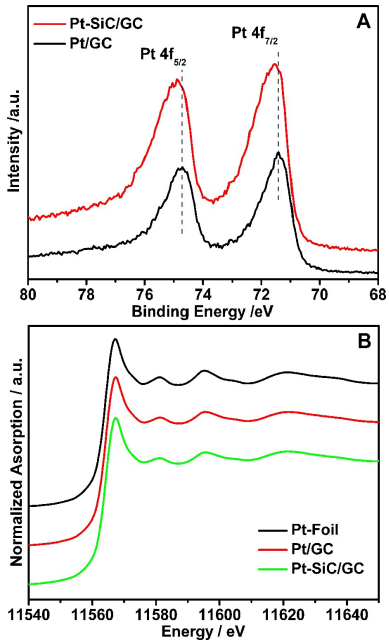

Fig. 5 (A) Pt4f XPS spectra for Pt-SiC/GC and Pt/GC composites; (B) XANES of Pt L_3-edge spectra for Pt foil, Pt/GC and Pt-SiC/GC.

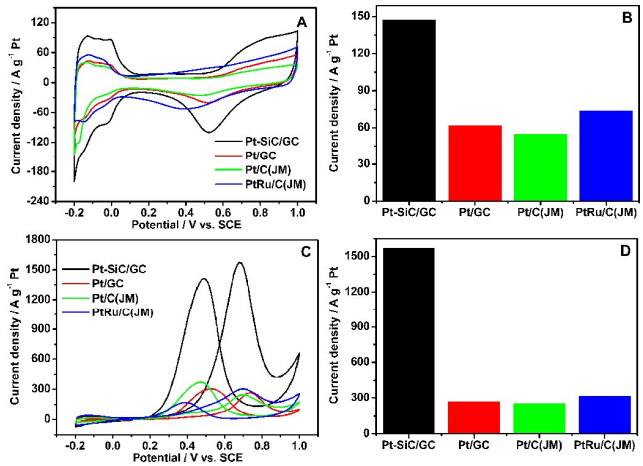

Fig. 6 Electrochemical performances: (a) The CV curves of Pt-SiC/GC, Pt/GC. Pt/C(JM) and PtRu/C(JM) catalysts in 0.5 M H_2SO_4 electrolyte; (b) The corresponding ECSA calculated based on (a). (c) The CV curves of Pt-SiC/GC, Pt/GC. Pt/C(JM) and PtRu/C(JM) catalysts in 0.5 M H_2SO_4 + 0.5 M CH_3OH electrolyte; (d) The corresponding mass ratio activity calculated based on (c).

Inspired by the attractive properties (close contact, well dispersion and small size), the Pt-SiC/GC catalyst is expected to exhibit promoted electrochemical performance. The electrocatalytic properties of the as-prepared Pt-SiC/GC catalyst were evaluated. To study the role of SiC component in the catalyst, the Pt/GC catalyst without SiC was also prepared for comparison. The accurate content of Pt metal in Pt/GC and Pt-SiC/GC catalysts determined by inductively coupled plasma (ICP) were about 9.86 wt% and 9.91 wt%, respectively. Besides, two kinds of commercial Pt/C (20 wt% Pt, JM) and PtRu/C (30 wt% PtRu, JM) catalysts were also tested for comparison. The cyclic voltammetry (CV) curves of the catalysts were recorded at room temperature in nitrogen-purged 0.5 M H_2SO_4 solutions at a sweep rate of 50 mV s^{-1} as shown in Fig. 6A. It can be seen that the typical CV curves of Pt with hydrogen adsorption/desorption regions and Pt oxidation/ reduction peaks are obtained for all the catalysts. The electrochemical active surface areas (ECSAs) of the catalysts were calculated and shown in Fig. 6B by measuring the charge collected in the hydrogen adsorption/desorption region after double-layer correction and assuming a value of 210 μC cm^{-2} for the adsorption of a hydrogen monolayer. Therefore, the specific ECSA (the ECSA per unit weight of Pt metal) of Pt-SiC/GC catalyst can be calculated as 147.1 m^2 g^{-1} Pt (Table 1), which is about 2.4, 2.7 and 2.3 times as these of the Pt/GC, Pt/C(JM) and PtRu/C(JM) catalysts, respectively.

Table 1 The electrochemical performance of the catalysts.

Catalysts	ECSA (m^2 g^{-1} Pt)	Peak potential (V)	Mass current density (A g^{-1} Pt)
Pt-SiC/GC	147.1	0.68	1585.3
Pt/GC	61.9	0.75	273.7
Pt-SiC/C	52.3	0.70	217.1
Pt/C(JM)	54.8	0.70	257.4
PtRu/C(JM)	63.7	0.71	316.5

The methanol oxidation reaction (MOR) measurements were performed in 0.5 M H_2SO_4 + 0.5 M CH_3OH electrolyte, and the CV curves after the cycle stabilized were shown in Fig. 6C. All the obtained currents were normalized by the mass of Pt loading. The CV curves consisted of two well-defined peaks at the forward and backward scans, which are attributed to the oxidation of methanol molecules and intermediates, respectively. The Pt-SiC/GC catalyst showed the highest current density of 1585.3 A g^{-1} Pt for MOR, which is much higher than those of Pt/GC (273.7 A g^{-1} Pt), commercially Pt/C(JM) (257.4 A g^{-1} Pt) and PtRu/C(JM) (316.5 A g^{-1} Pt) (Fig. 6D). The previous study demonstrated that the reverse scan of CV curve is attributed to oxidation of mediate incomplete products, including CO, COOH and CHO.[27,41] The excellent performance of Pt-SiC/GC can be attributed to the synergistic effect and intimate contact between SiC and Pt, which could be evidenced by the above TEM, XPS and XANES analytic results. Electrochemical impedance spectroscopy (EIS) was used to estimate the charge transfer resistance of the different electrodes in electrolyte. As shown in Fig. S14, the impedance arc of SiC/GC support is larger than that of the GC, indicating the

charge transfer resistance of SiC/GC is much larger than that of the GC. However, after loading Pt NPs, the impedance arc of Pt-SiC/GC is smaller than that of Pt/GC, implying the charge transfer resistance of the Pt-SiC/GC electrode is much smaller than that of the Pt/GC. This phenomenon is attributed to synergistic effect could bring the electron transfer from Pt to SiC, which can be proved by the XPS results.

For comparing the effect of size and content of SiC in the composite on the electrocatalytic performance, the SiC/GC synthesized from different heating temperatures were also used as support for Pt catalyst. Fig. S15 and Table S5 displayed that the Pt-SiC/GC-1300 and Pt-SiC/GC-1500 catalysts exhibit much lower ECSA and lower current density towards MOR compared with that of Pt-SiC/GC catalyst, demonstrating the small size of SiC NPs is more favorable to the intimate contact and develop of synergistic effect between SiC and Pt NPs. To study the effect of electronic conductivity of supports on the electrochemical performance of catalyst, the sample of SiC/amorphous carbon (SiC/C) composite synthesized without using $FeCl_3$ catalyst were also prepared for comparison (see experiment section and Table S2). As a support, the Pt-SiC/C with 10 wt% Pt loading catalyst exhibits a lowest current density for MOR (only about 0.14 time as that of Pt-SiC/GC catalyst, Fig. S16), which further prove the electron conductivity of crystalline carbon nanosheets in SiC/GC would benefit to the electrons transfer in the MOR. Encouragingly, the present Pt-SiC/GC catalyst almost shows the highest electrocatalytic activity among a series of carbide (nitride)-based supported Pt anodic catalysts of DMFC, such as SiC, SiC/C, SiC/porous carbon, WC (WN)/RGO or mesoporous carbon, WC (Mo_2C)/GC, VC_x/C, CrN, NbC or TiC nanowires (see Table S6 in supporting information), which require higher Pt loadings. Importantly, our present Pt-SiC/GC catalyst exhibits the higher current density, meanwhile, possesses the lower Pt loading, indicating the potential application in DMFC.

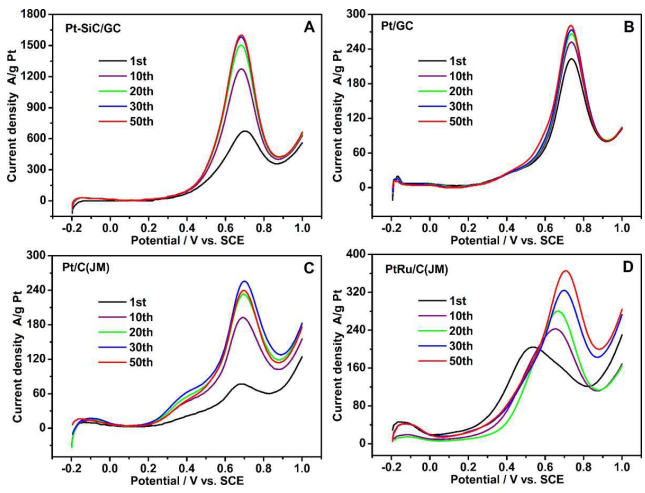

Fig. 7 Stability test: CV curves of different cycle numbers for (A) Pt-SiC/GC, (B) Pt/GC, (C) Pt/C(JM) and (D) PtRu/C(JM) catalysts in 0.5 M H_2SO_4 + 0.5 M CH_3OH electrolyte.

Catalyst stability plays the vital role in commercial applications. Fig. 7 displays the CVs of MOR for different cycle numbers. It can be observed that the onset and peak potentials for MOR on PtRu/C(JM) gradually shift to positive direction with the increasing of cycle number. The poor durability for PtRu/C(JM) catalyst is because of the dissolution of Ru atoms in the process of electrochemical scan. Compared with Pt/C(JM) and PtRu/C(JM) catalysts, the current density for Pt-SiC/GC and Pt/GC could stabilize after 30 cycles, and the Pt-SiC/GC catalyst exhibits the largest current density towards MOR.

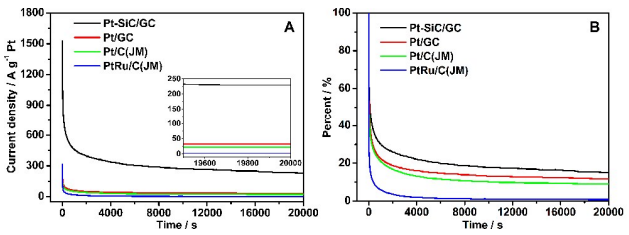

Fig. 8 Chronoamperometric curves of Pt-SiC/GC, Pt/GC, Pt/C(JM) and PtRu/C(JM) catalysts at 0.5 V in 0.5 M H_2SO_4 + 0.5 M CH_3OH electrolyte for 20000 s.

The chronoamperometric (CA) curve is an effective method to evaluate the electrocatalytic activity and stability of catalysts. The typical current density–time responses for MOR measured at a potential of 0.5 V for Pt-SiC/GC, Pt/GC, Pt/C(JM) and PtRu/C(JM) catalysts were shown in Fig. 8. It can be observed that the decay current density decrease rapidly in the beginning for all the four electrocatalysts owing to the formation of reactive intermediates such as CO_{ads}, $COOH_{ads}$ and CHO_{ads} during the MOR. Notably, Pt-SiC/GC shows higher initial and higher limiting current density, and also higher current density retention (229.5 A g^{-1} Pt, 19.3 %) after 20000 s measurement than other three catalysts, indicating excellent catalytic activity and stability. Therefore, the obtained Pt–SiC/GC catalyst should be more potential application in DMFC.

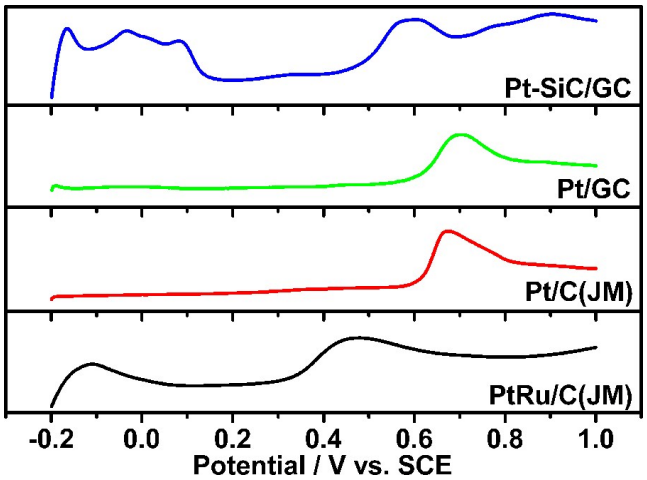

Fig. 9 CO stripping voltammograms of Pt-SiC/GC, Pt/GC, Pt/C(JM) and PtRu/C(JM) catalysts in 0.5 M H_2SO_4 electrolyte at a scan rate of 50 mV s^{-1}.

CO electro-oxidation potential is one of the key properties for determining the catalytic activity towards MOR owing to CO oxidation reaction is a slow step during MOR. To further

investigate the catalytic activity of catalysts, the CO stripping voltammograms was performed in 0.5 M H_2SO_4 electrolyte. As shown in Fig. 9, the PtRu/C(JM) catalyst exhibits the lowest onset potential and peak potential owing to the bifunctional mechanism. In addition, the Pt-SiC/GC displays a peak of CO_{ads} oxidation at E_{CO} = 0.58 V, which is lower than that of the Pt/GC (E_{CO} = 0.69 V) and Pt/C(JM) (E_{CO} = 0.67 V). The negative shift of E_{CO} on Pt-SiC/GC catalyst indicates that the incorporation of SiC with Pt plays an important role for improving the CO tolerance of elelctrocatalysts, demonstrating the promising candidate of Pt-SiC/GC as the catalyst for long-term operational DMFC.

4. Conclusions

In summary, we report that SiC/GC nanocomposite promotes the activity and stability of Pt electrocatalyst in MOR. The electron transfer from Pt to SiC is beneficial to develop the synergistic effect. The SiC/GC supported 10 wt% Pt catalyst (Pt-SiC/GC) showed a greater ECSA, higher electrocatalytic activity, better durability and greater CO tolerance than a commercial 20 wt% Pt/C(JM) and 30 wt% PtRu/C(JM) catalysts toward MOR. This improved performance is mainly due to the high corrosion resistance of the SiC/GC support, coupled with a synergistic behavior and intimate contact among Pt, SiC and GC, that allows faster oxidation of mediate species produced during the MOR. The Pt loading in the Pt-SiC/GC catalyst is only 10 wt% that could sharply decrease the cost of DMFCs, making it one of the most efficient catalysts ever reported for MOR. The present method provides a promising and alternative approach for the design of SiC/GC supports, which could be used to prepare high performance catalysts and could potentially replace the traditional Pt/C catalyst in DMFCs.

Acknowledgements

We gratefully acknowledge the support of this research by the National Natural Science Foundation of China (No. 21371053, 21401048, 21376065, 21571054), the China Postdoctoral Science Special Foundation (No. 2015T80374), the China Postdoctoral Science Foundation (No. 2014M551285), the Postdoctoral Science Foundation of Heilongjiang Province (No. LBH-TZ0519), Harbin science and technology innovation talents research Foundation (2015RAQXJ057), the application technology research and development projects in Harbin (No. 2013AE4BW051), Innovative Research Project of Key Laboratory of Functional Inorganic Material Chemistry, Ministry of Education.

References

1 K. Debe, *Nature*, 2012, **486**, 43–51.
2 X. Shan, D. P. Ismael, L. J. Wang, P. Wiktor, Y. Gu, L. H. Zhang, W. Wang, J. Lu, S. P. Wang, Q. H. Gong, J. H. Li and N. J. Tao, *Nat. Nanotechnol.*, 2012, **7**, 668.
3 S. G. Chen, Z. D. Wei, X. Q. Qi, L. C. Dong, Y. G. Guo, L. J. Wan, Z. G. Shao and L. Li, *J. Am. Chem. Soc.*, 2012, **134**, 13252.
4 L. Wei, Y.-J. Fan, J.-H. Ma, L.-H. Tao, R.-X. Wang, J.-P. Zhong and H. Wang, *J. Power Sources*, 2013, **238**, 157.
5 R.-X. Wang, Y.-J. Fan, L. Wang, L.-N. Wu, S.-N. Sun and S.-G. Sun, *J. Power Sources*, 2015, **287**, 341.
6 R.-X. Wang, J.-J. Fan, Y.-J. Fan, J.-P. Zhong, L. Wang, S.-G. Sun and X.-C. Shen, *Nanoscale*, 2014, **6**, 14999.
7 H.-H. Li, S. Zhao, M. Gong, C.-H. Cui, D. He and H.-W. Liang, *Angew. Chem. Int. Ed.*, 2013, **52**, 7472.
8 L. Ruan, E. Zhu, Y. Chen, Z. Lin, X. Huang, X. Duan and Y. Huang, *Angew. Chem. Int. Ed.*, 2013, **52**, 12577.
9 L. Wang, Y. Nemoto and Y. Yamauchi, *J. Am. Chem. Soc.*, 2011, **133**, 9674.
10 B. Lim, M. J. Jiang, P. H. C. Camargo, E. C. Cho, J. Tao, X. M. Lu, Y. M. Zhu and Y. N. Xia, *Science*, 2009, **324**, 1302.
11 A. Rabis, P. Rodriguez and T. J. Schmidt, *ACS Catal.*, 2012, **2**, 864.
12 S. H. Joo, J. Y. Park, C.-K. Tsung, Y. Yamada, P. Yang and G. A. Somorjai, *Nat. Mater.*, 2009, **8**, 126.
13 C. Cui, L. Gan, M. Heggen, S. Rudi and P. Strasser, *Nat. Mater.*, 2013, **12**, 765.
14 B. T. Sneed, A. P. Young, D. Jalalpoor, M. C. Golden, S. Mao, Y. Jiang, Y. Wang and C.-K. Tsung, *ACS Nano*, 2014, **8**, 7239.
15 C. Chen, Y. Kang, Z. Huo, Z. Zhu, W. Huang, H. L. Xin, J. D. Snyder, D. Li, J. A. Herron, M. Mavrikakis, M. Chi, K. L. More, Y. Li, N. M. Markovic, G. A. Somorjai, P. Yang and V. R. Stamenkovic, *Science*, 2014, **343**, 1339.
16 B. Y. Xia, H. B. Wu, N. Li, Y. Yan, X. W. Lou and X. Wang, *Angew. Chem. Int. Ed.*, 2015, **54**, 3797.
17 H. L. Xin, S. Alayoglu, R. Tao, A. Genc, C.-M. Wang, L. Kovarik, E. A. Stach, L.-W. Wang, M. Salmeron, G. A. Somorjai and H. Zheng, *Nano Lett.*, 2014, **14**, 3203.
18 Y. Jia, Y. Jiang, J. Zhang, L. Zhang, Q. Chen, Z. Xie and L. Zheng, *J. Am. Chem. Soc.*, 2014, **136**, 3748.
19 F. Saleem, B. Xu, B. Ni, H. Liu, F. Nosheen, H. Li and X. Wang, *Adv. Mater.*, 2015, **27**, 2013.
20 Y. Yu, W. Yang, X. Sun, W. Zhu, X.-Z. Li, D. J. Sellmyer and S. Sun, *Nano Lett.*, 2014, **14**, 2778.
21 D. Y. DeSario and F. J. DiSalvo, *Chem. Mater.*, 2014, **26**, 2750.
22 R. B. Levy and M. Boudart, *Science*, 1973, **181**, 547.
23 S. B. Yin, M. Cai, C. X. Wang and P. K. Shen, *Energy Environ. Sci.*, 2011, **4**, 558.
24 R. H. Wang, C. Tian, L. Wang, B. L. Wang, H. Zhang and H. Fu, *Chem. Commun.*, 2009, 3104.
25 Z. Yan, G. He, P. K. Shen, Z. Luo, J. Xie and M. Chen, *J. Mater. Chem. A*, 2014, **2**, 4014.
26 G. He, Z. Yan, X. Ma, H. Meng, P. K. Shen and C. Wang, *Nanoscale*, 2011, **3**, 3578.
27 X. Y. Tao, Y. P. Li, J. Du, Y. Xia, Y. C. Yang, H. Huang, Y. P. Gan, W. K. Zhang and X. D. Li, *J. Mater. Chem.*, 2011, **21**, 9095.
28 X. Y. Tao, J. Du, Y. P. Li, Y. C. Yang, Z. Fan, Y. P. Gan, H. Huang, W. K. Zhang, L. X. Dong and X. D. Li, *Adv. Energy Mater.*, 2011, **1**, 534.
29 H. Yan, C. Tian, L. Sun, B. Wang, L. Wang, J. Yin, A. Wu and H. Fu, *Energy Environ. Sci.*, 2014, **7**, 1939.
30 J. Yang, Y. Xie, R. Wang, B. Jiang, C. Tian, G. Mu, J. Yin, B. Wang and H. Fu, *ACS Appl. Mater. Interfaces*, 2013, **5**, 6571.
31 R. Wang, Y. Xie, K. Shi, J. Wang, C. Tian, P. Shen and H. Fu, *Chem. Eur. J.*, 2012, **18**, 7443.
32 C. Eddy and D. Gaskill, *Science*, 2009, **324**, 1398.
33 S. N. Stamatin, J. Speder, R. Dhiman, M. Arenz and E. M. Skou, *ACS Appl. Mater. Interfaces*, 2015, **7**, 6153.

34 M. Dasog, L. F. Smith, T. K. Purkait and J. G. C. Veinot, *Chem. Commun.*, 2013, **49**, 7004.
35 H. Weishart, V. Heera, F. Eichhorn, B. Pécz, A. Barna and W. Skorupa, *Diamond Relat. Mater.*, 2003, **12**, 1241.
36 H. Wang, I. Sung, X. Li and D. Kim, *J. Porous Mater.*, 2004, **11**, 265.
37 J. Y. Fan, X. L. Wu and P. K. Chu, *Prog. Mater. Sci.*, 2006, **51**, 983.
38 R. Dhiman, E. Johnson, E. M. Skou, P. Morgen and S. M. Andersen, *J. Mater. Chem. A*, 2013, **1**, 6030.
39 L. Sun, C. Tian, M. Li, X. Meng, L. Wang, R. Wang, J. Yin and H. Fu, *J. Mater. Chem. A*, 2013, **1**, 6462.
40 B. Ravel and M. Newville, *J. Synchrotron Radiat.*, 2005, **12**, 537.
41 L. Wang, G. Mu, C. Tian, L. Sun, W. Zhou, P. Yu, J. Yin and H. Fu, *ChemSusChem*, 2013, **6**, 880.
42 J. Fan, H. Li, J. Jiang, K. Y. So, Y. W. Lam and P. K. Chu, *Small*, 2008, **4**, 1058.
43 J. Fan and P. K. Chu, *Small*, 2010, **6**, 2080.
44 L. Wang, C. Tian, H. Wang, Y. Ma, B. Wang and H. Fu, *J. Phys. Chem. C*, 2010, **114**, 8727.

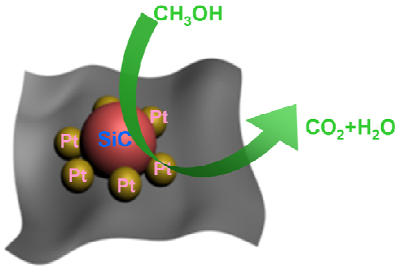

SiC/graphitic carbon nanosheets (SiC/GC) nanocomposite with 17 nm SiC nanoparticles dispersed on GC uniformly was synthesized via a novel vaporization-deposition-reduction strategy derived from coconut shell and silica ceramic chip. Owing to the electron transfer from Pt to SiC is beneficial to develop the synergistic effect, the SiC/GC supported 10 wt% Pt catalyst (Pt-SiC/GC) showed superior electrocatalytic performance toward MOR.